A venturi-shaped roof for wind-induced natural ventilation of buildings: wind tunnel and CFD evaluation of different design configurations

T. van Hooff [(a,b)], B. Blocken * [(a)] , L. Aanen [(c)] , B. Bronsema [(d)]

(a) Building Physics and Systems, Eindhoven University of Technology, P.O. box 513, 5600 MB Eindhoven, the Netherlands
(b) Division of Building Physics, Department of Civil Engineering, Katholieke Universiteit Leuven, Kasteelpark Arenberg 40, P.O. Box 2447, 3001 Leuven, Belgium
(c) Peutz BV, P.O. box 66, 6585 ZH, Mook, The Netherlands
(d) Faculty of Architecture – Department of Climate Design, Delft University of Technology, Prof. Boerhaaveweg 37, 2251 HX Voorschoten, The Netherlands

Abstract
Wind tunnel experiments and Computational Fluid Dynamics (CFD) are used to analyse the flow conditions in a venturi-shaped roof, with focus on the underpressure in the narrowest roof section (contraction). This underpressure can be used to partly or completely drive the natural ventilation of the building zones. The wind tunnel experiments are performed in an atmospheric boundary layer wind tunnel at scale 1:100. The 3D CFD simulations are performed with steady RANS and the RNG k-ε model. The purpose of this study is twofold: (1) to evaluate the accuracy of steady RANS and the RNG k-ε model for this application and (2) to assess the magnitude of the underpressures generated with different design configurations of the venturi-shaped roof. The CFD simulations of mean wind speed and surface pressures inside the roof are generally in good agreement (10-20%) with the wind tunnel measurements. The study shows that for the configuration without guiding vanes, large negative pressure coefficients are obtained, down to -1.35, with reference to the free-stream wind speed at roof height. The comparison of design configurations with and without guiding vanes shows an – at least at first sight – counter-intuitive result: adding guiding vanes strongly decreases the absolute value of the underpressure. The reason is that the presence of the guiding vanes increases the flow resistance inside the roof and causes more wind to flow over and around the roof, and less wind through it (wind-blocking). As a result, the optimum configuration is the one without guiding vanes.

Keywords: Computational Fluid Dynamics (CFD); sustainable building; natural ventilation; energy efficiency; venturi-effect; airflow

1. Introduction

Natural ventilation is a sustainable approach to achieve a healthy and comfortable indoor environment in buildings. One of the most important influencing parameters concerning the feasibility of natural ventilation of buildings is the geometry of the building itself. In the past, several studies have been conducted to improve the natural ventilation of a building by modifying the building facades (e.g. wind floors, double-skin facades) or by adding structures on the roof of a building (e.g. wind towers, wind catchers). An overview of wind-driven ventilation techniques is provided by Khan et al. [1]. The present study consists of the analysis of the aerodynamic performance of a venturi-shaped roof that was designed by Bronsema as part of the research project "Earth, Wind & Fire – Air-conditioning powered by Nature" [2] (Fig. 1). The roof consists of a disk-shaped roof construction that is positioned at a certain height above the actual building, creating a contraction that is expected to provide significant negative pressures that can be used to partly or completely drive the natural ventilation of the building.

Analysis of natural ventilation of buildings can be performed using a wide range of methods [3], including: (1) reduced-scale water tank experiments (e.g. [4-6]); (2) analytical and/or semi-empirical formulae (e.g. [4,7-9]); (3) full-scale measurements (e.g. [10-13]); (4) reduced-scale atmospheric boundary layer wind tunnel experiments (e.g. [14-17]); and (5) numerical simulation with Computational Fluid Dynamics (CFD) (e.g. [6,10,13,14,18-20]). Water tank experiments and analytical formulae have generally been applied for simplified configurations and have proved very valuable to gain insight in the process of natural ventilation, such as the

---

* **Corresponding author**: Bert Blocken, Building Physics and Systems, Eindhoven University of Technology, P.O.Box 513, 5600 MB Eindhoven, the Netherlands. Tel.: +31 (0)40 247 2138, Fax +31 (0)40 243 8595
E-mail address: b.j.e.blocken@tue.nl

combined effects of wind and buoyancy as driving forces (e.g. [5,7]). They are however less suitable for practical applications for specific buildings in specific environments. For such applications, full-scale measurements are very valuable but they are generally time-consuming and expensive and the boundary conditions are often uncontrollable. In addition, full-scale measurements are not an option in the design phase of buildings. Wind tunnel experiments allow much better control of the boundary conditions. However, they strictly need to be performed in an atmospheric boundary layer wind tunnel, with a sufficiently long upstream fetch to establish appropriate atmospheric boundary layer profiles. Additionally, scaling of the model geometry can be a problem, especially for small openings in which, when scaled down, the Re numbers can drop below the threshold for fully turbulent flow. In that case – among others – CFD is an interesting option [13]. CFD has the advantage that it allows full control over the boundary conditions, that it provides data in every point of the domain simultaneously ("whole-flow field data") and that it does not suffer from scaling limitations because simulations can be performed at full scale. It also allows efficient parametric analysis of different design configurations (e.g. [13]). However, the accuracy of CFD is an important concern and solution verification and validation studies are imperative [21].

In this paper, the aerodynamic performance of the venturi-shaped roof concept is analysed by a combination of wind tunnel measurements and CFD simulations. The purpose of the study is twofold: (1) to evaluate the accuracy of steady RANS CFD and the RNG k-ε model for this application and (2) to assess the magnitude of the underpressures in the contraction and to compare the performance of different design configurations. Three different wind roof configurations are assessed in terms of the negative pressure at position E in the contraction (see Fig. 1). Note that the concept of the wind roof design to some extent resembles that of the wind floor that has been applied in the Liberty Tower of Meiji University in Japan [22] and the wind roof of GSW headquarters in Berlin, Germany [23] to increase the natural ventilation of high-rise buildings.

First, the building and roof geometry are described. Next, the wind tunnel measurements are outlined, followed by the CFD simulations. Finally, the results of the wind tunnel measurements and CFD simulations will be presented and compared, and topics for future work will be discussed.

2. Description of building and roof geometry

The study is conducted for a rectangular (20 m x 20 m) building with a height of 50 m, measured up to the edge of the roof (Fig. 1a). The venturi-shaped roof consists of two parts. The lower part is constructed from half a "square disk" with dimensions 23.4 m x 23.4 m x 2 m (L x W x H) and it is positioned directly on top of the building, this way creating a roof overhang of 1.7 m on each side of the building, at which ventilation inlets will be placed. At a distance 'c' above this part of the roof a full "square disk" is positioned with dimensions 23.4 m x 23.4 m x 4 m (L x W x H), resulting in a nozzle-shaped roof entrance from all four sides of the building. This part can be supported by e.g. a set of slender vertical columns or by the guiding vanes, which will be discussed further. In this study, the distances 'b' and 'c' in Fig. 1 are taken equal to 5 m and 1 m, respectively, yielding a contraction ratio of 5. 'c' is the height of the narrowest part of roof contraction. The position of interest inside the roof is indicated with the letter E (from "exhaust") in Figure 1a and b. In this study, the exhaust is considered to be closed and the surface pressure at this position will be evaluated. A reasonable expectation is that at this position, the flow speed will have increased due to the decrease of the cross-sectional area of the contraction, which will locally yield increased negative pressures. While this could be called "venturi-effect", it is important to note that strictly, the term venturi-effect refers to confined flows, while in the case of this roof, the air can also flow over and around the roof, rather than only through it. It will therefore generally not be true that the flow speed in the contraction is inversely proportional to the cross-sectional area, as it would be in a confined flow. This discussion is similar to the one for wind flow in passages between parallel buildings [24] and for wind flow in passages between buildings in converging and diverging arrangement [25,26]. In the present study, we will use the term "venturi-effect" to refer to the expected increase of flow speed and underpressure, in spite of the non-confined flow conditions.

In an attempt to enhance the venturi-effect, guiding vanes could be added between the lower part and the upper part of the roof opening. Two configurations of guiding vanes are studied: (a) 4 guiding vanes (one at every 90° interval), or (b) 36 guiding vanes (one at every 10° interval) (Fig. 1b). For both configurations, the resulting opening 'f' in the centre of the roof has dimensions 2 x 2 m^2 (L x W) (see Fig. 1). Overall, three configurations are studied in detail (Fig. 2):

- Configuration A: venturi-shaped roof without guiding vanes;
- Configuration B: venturi-shaped roof with guiding vanes every 90°;
- Configuration C: venturi-shaped roof with guiding vanes every 10°.

In addition, a fourth configuration (D) is briefly included, to serve as a reference case. It is the same building but without venturi-shaped roof (i.e. only half a "square disk" and no "full" square disk above it). All experiments and simulations are conducted for an isolated building, i.e. without surrounding buildings. Therefore, all

differences in velocities and surface pressures between the different configurations are only due to changes in the wind roof design.

3. Wind tunnel measurements

A reduced-scale model (1:100) of the building with venturi-shaped roof is constructed and placed in the closed-circuit atmospheric boundary layer (ABL) wind tunnel (Fig. 3) at Peutz BV in Mook, the Netherlands. The dimensions of the test section are 3.2 x 1.8 m^2 (W x H), resulting in a blockage ratio of about 2%. The building model was placed on a turntable with a diameter of 2.3 m. The measurement positions on the building and roof surfaces and in the roof are schematically indicated in Figure 4. Surface pressures are measured at 24 positions on the four vertical facades, at 8 positions on the inclined facade parts (ventilation inlets) and at 26 positions in the roof contraction. The measurements are performed with HCLA12X5EB amplified differential pressure sensors from Sensortechnics. Wind speed is measured at 7 positions inside the roof contraction using NTC resistor elements. All wind speed measurements are made at mid-height in the contraction. The NTCs are operated with a constant current and are calibrated by Peutz by determining the relationship between wind speed and temperature (and corresponding resistance) of each individual probe. The probes are not direction-sensitive and due to the relatively long reaction time of the probes, only average wind speeds can be measured, with an accuracy of ±10%. Approach-flow vertical profiles of mean wind speed U and turbulence intensity I_u are measured at the edge of the turntable using hot-wire anemometers and are presented in Figure 5. The measured wind speed profile can be described by a logarithmic law with a friction velocity $u^* = 0.956$ m/s and an aerodynamic roughness length $y_0 = 0.005$ m (full scale: $y_0 = 0.5$ m). The incident reference wind speed at roof height (0.5 m) is 10.5 m/s. Measurements are made for four wind directions: $\varphi = 0°$, 15°, 30° and 45°, taking into account the symmetry of the building and the building roof.

4. CFD simulations: computational model and computational parameters

4.1. Computational geometry and grid

A computational model was made of the reduced-scale building model used for the wind tunnel measurements. The same scale was used for validation purposes. The computational domain has dimensions L x B x H = 10.2 m x 10.2 m x 3 m (Fig. 6a). This domain shape allows modelling different wind directions (0° to 45°). A lot of effort has been devoted to construct high-quality and high-resolution computational grids (Fig. 6b and Fig. 7). The grids have at least 10 cells between each two adjacent surfaces, such as the guiding vanes, as requested by the best practice guidelines by Franke et al. [27] and Tominaga et al. [28]. The grids are made using the grid generation technique presented by van Hooff and Blocken [13]. In this technique, the geometry and the grid are created simultaneously, by a series of extrusion operations. This procedure allows a large degree of control over the size and shape of the cells, and therefore of the quality and resolution of the computational grid. It allows high-quality grids to be made, even for rather complex geometries. The same technique has been used successfully on previous occasions to model sport stadium geometries [13,20,29]. The four grids are block-structured and consist of 2.0 million, 2.4 million, 3.3 million and 1.8 million hexahedral cells for configurations A, B, C and D, respectively. Note that the grids do not contain any pyramidal or tetrahedral cells. Special attention was paid to the detailed reproduction and meshing of the wind roof geometry. A high grid resolution is applied in the proximity of the roof in view of the expected large flow gradients. A detailed grid-sensitivity analysis was performed indicating that the grids shown in Figure 7 provide nearly grid-independent results. The grid-sensitivity analysis will be reported in section 5.1.

4.2. Boundary conditions

At the inlet of the domain the measured approach-flow mean wind speed profile is imposed. Turbulent kinetic energy k is calculated from the turbulence intensity I_u using $k = 0.5(I_u.U)^2$. The turbulence dissipation rate $\varepsilon = (u^*)^3/\kappa(y+y_0)$, where y is the height coordinate, κ the von Karman constant ($\kappa = 0.42$) and u^* the friction velocity related to the logarithmic mean wind speed profile. At the ground and building surfaces, the standard wall functions by Launder and Spalding [30] are used with the sand-grain based roughness modification by Cebeci and Bradshaw [31]. For the ground surface, the parameters k_S and C_S, to be used in Fluent [32], should be selected to correctly represent the rough fetch upstream of the building model (see Fig. 3a). This type of consistent atmospheric boundary layer simulation is very important to obtain accurate simulation results [24,33]. Therefore, k_S and C_S have to be determined using their appropriate consistency relationship with y_0. This relationship was derived by Blocken et al. [33] for Fluent and CFX. For Fluent 6, up to at least version 6.3, it is given by $k_S = 9.793y_0/C_S$. The combination $k_S = 0.0098$ m and $C_S = 5$ m is selected. The building surfaces are

assumed to be smooth ($k_S = 0$ m and $C_S = 0.5$). Zero static pressure is imposed at the outlet of the domain and the top of the domain is modeled as a slip wall (zero normal velocity and zero normal gradients of all variables).

4.3. Solver settings

The 3D Reynolds-averaged Navier-Stokes (RANS) equations are solved in combination with the Renormalisation Group (RNG) k-ε turbulence model [34], using Fluent 6.3.26. The RNG k-ε turbulence model was chosen for this study because of its good performance in predicting the surface pressures on the windward building facades and in the roof opening in a preliminary study, and because of its superior performance in an earlier study by Evola and Popov [35]. Pressure-velocity coupling is taken care of by the SIMPLE algorithm, pressure interpolation is standard and second-order discretization schemes are used for both the convection terms and the viscous terms of the governing equations. Convergence has been monitored carefully and the iterations have been terminated when all residuals showed no further reduction with increasing number of iterations. At this stage, the scaled residuals were: 10^{-4} for continuity, 10^{-7} for momentum, 10^{-6} for turbulent kinetic energy and 10^{-4} for turbulence dissipation rate.

5. Results

5.1. Grid-sensitivity analysis

To reduce numerical errors, not only iterative convergence but also grid convergence should be assessed. In this study, a grid-sensitivity analysis was performed by constructing two additional grids for the configurations A and C: a coarser grid and a finer grid. Coarsening and refining was performed with an overall linear factor $\sqrt{2}$. The model for configuration A (no guiding vanes) has 549,380 cells for the coarse grid, 2,041,268 cells for the middle grid and 4,364,688 cells for the fine grid. The model for configuration C (guiding vanes every 10°) has 2,040644 cells for the coarse grid, 3,250,032 cells for the middle grid and 7,107,648 cells for the fine grid. The resulting grids for configuration A are shown in Fig. 8a. The results on the three grids are compared in terms of the mean wind speed along a vertical line in the centre of the roof contraction (Fig. 8b), indicating only a very limited dependence of the results on the grid resolution. The results on the three grids are also compared in terms of the absolute values of the pressure coefficients at the windward building facade and in the centre of the roof contraction (Fig. 8c-d). Note that the pressure coefficients are computed as $C_p = (P-P_0)/(0.5\rho U_{ref}^2)$ with P the static pressure at the surface, P_0 the reference static pressure, $\rho = 1.225$ kg/m³ the air density and U_{ref} the reference wind speed at roof height ($U_{ref} = 10.5$ m/s at y = 0.5 m). A small deviation (7 %) is found between the coarse and middle grid for the C_p at position E, while almost no deviation is found for the value of this parameter between the middle grid and the fine grid. Similar results are obtained for configuration C. Therefore, the middle grids (i.e. those shown in Fig. 7) are retained for further analysis.

5.2. Model-scale versus full-scale CFD simulations

Most CFD simulations presented in this paper have been performed at model scale (i.e. wind tunnel scale). To assess their validity in reality, i.e. at full scale, some simulations at full scale have been conducted. The results from both sets are compared in Figure 9, for the configuration without guiding vanes and the configuration with guiding vanes every 10°. The differences between the values of the mean underpressure and the mean wind speed in the centre of the roof contraction are very limited. Only for C_p and configuration C, the difference is about 10%. The model scale Reynolds numbers are 10400 and 6850 for configurations A and C, respectively. Apparently, these numbers are large enough to provide a sufficient degree of Reynolds number independence.

5.3. Comparison of CFD and wind tunnel results

The presentation of the CFD and wind tunnel results and their comparison is performed in three parts. First, the pressure coefficients at the windward vertical facades and at the windward inclined facade parts are presented. Next, the wind speed ratio U/U_{ref} at mid-height in the centre of the roof contraction is shown. Finally, the pressure coefficients at position E in the centre of the roof contraction are displayed.

Figure 10 compares the numerically simulated and measured pressure coefficients at the windward facades of the configurations A, B and C and for the four wind directions: $\varphi = 0°$, 15°, 30°, and 45°. Only the windward facades are considered, because it is known that steady RANS CFD is deficient in reproducing the wind flow downstream of windward facades [36,37]. This deficiency is considered less important for the present study, because the actual focus is on the flow conditions inside the roof contraction. For the windward facades, the general agreement is quite good, although there seems to be a systematic overestimation of the measurement

4

values by the CFD results, by about 10%. Possible reasons for this are the performance of the RNG model and/or streamwise gradients in the approach-flow mean wind speed and turbulence intensity profile due to the smooth turntable. Note that the smooth part of the turntable, between the roughness elements and the position of the building model, was modelled as a rough surface in CFD, while it is actually not covered by roughness elements in the experiment. Therefore, in the wind tunnel, horizontally inhomogeneous profiles are present, which can affect the accuracy of the results.

Fig. 11 compares the numerically simulated and measured mean wind speed ratios U/U_{ref} at mid-height in the centre of the roof contraction, for the three roof configurations and for the four wind directions. The deviations are generally smaller than 10%, which is considered a very close agreement. Note that the CFD results all slightly underestimate the mean wind speed ratio compared to the wind tunnel results.

Fig. 12 compares the numerically simulated and measured pressure coefficients C_p at position E in the centre of the roof contraction. For $\varphi = 0°$ and $\varphi = 15°$, the CFD results and the wind tunnel results are in fairly good agreement. The agreement however deteriorates for the more oblique wind directions, $\varphi = 30°$ and $45°$. The reasons are (1) the specific geometry of the roof, with four "ribs" on the roof surfaces (see e.g. Fig. 1 and 2); (2) the flow separation at the vanes, which is more pronounced for the oblique wind directions; and (3) the large C_p gradients at the roof surfaces. In spite of these deviations between the numerical and the measured C_p values, the trends are clear and allow a comparison of the performance of the different roof configurations.

5.4. Comparison of roof configurations

Fig. 10 shows that there are no clear differences between the different roof configurations in terms of C_p on the windward vertical and inclined facade parts. On the other hand, very clear differences are found for the wind speed ratio U/U_{ref} in Fig. 11. The ratio for the configuration without guiding vanes is about 50% higher than with guiding vanes. The configuration with guiding vanes every 90° only provides a slightly higher wind speed ratio than the one with guiding vanes every 10°. The parameter that is of most interest however is the pressure coefficient at the intended exhaust opening E, i.e. at the bottom centre of the roof contraction. Fig. 12 shows that a strong negative pressure coefficient is obtained for the configuration without guiding vanes: the numerically simulated C_p value ranges between -1.05 and -1.33, while the measured C_p value ranges between -1.20 and -1.35. For the configurations with guiding vanes however, much less negative C_p values obtained, which are at best (i.e. for $\varphi = 0°$) only about 30% of those for the configuration without guiding vanes. For $\varphi = 15°$, the values drop to less than 25% of those without guiding vanes. And for $\varphi = 30°$ and $45°$, the values either drop even further, or become positive. Both the numerical and the experimental results show the superior performance of the configuration without guiding vanes.

6. Discussion

The discussion focuses on three issues: (1) the calculation of the approach-flow turbulent kinetic energy profile from the measured turbulence intensity; (2) the reasons for the superior performance of the roof configuration without guiding vanes; and (3) the limitations of the present study.

The approach-flow turbulent kinetic energy k was calculated from the measured turbulence intensity I_u using the equation $k = 0.5(I_u.U)^2$. The reason for this is that I_u is the turbulence intensity measured by a single horizontally oriented hot wire. It therefore not only includes the contribution by the streamwise turbulent fluctuations but also part of the vertical turbulent fluctuations. When I_u would be the streamwise turbulence intensity only, the equation $k = (I_u.U)^2$ would probably have been more appropriate [28]. Nevertheless, the calculation of k from I_u in the present study is a source of uncertainty. Therefore, the effect of using different equations to calculate k from I_u on the calculated wind speed ratio U/U_{ref} and on the underpressure at position E was assessed, for configuration A. The effect on the ratio U/U_{ref} is less than 1% and therefore considered insignificant. The effect on the underpressure coefficient however is larger: for $k = 0.5(I_u.U)^2$, $C_p = -1.21$; for $k = (I_u.U)^2$, $C_p = -1.30$; for $k = 1.5(I_u.U)^2$, $C_p = -1.35$. Note however that $k = 0.5(I_u.U)^2$ is considered the best choice for the present study, and that the related uncertainty does not compromise the conclusions of the study.

Both the numerical and the experimental results show the – at least at first sight – counter-intuitive result that the configuration without guiding vanes yields a much larger underpressure in the centre of the roof contraction than the configurations with guiding vanes. Note that the intention of adding guiding vanes was to increase the magnitude of the underpressure, but that their presence actually has the opposite effect. The reason for this is twofold. First, while it could be expected that the guiding vanes provide a smoother conduction of the flow through the roof contraction, they actually represent multiple locations of flow separation, which is associated with momentum losses and flow speed reduction. Second, and more importantly, the presence of guiding vanes adds a considerable resistance to the flow through the roof contraction. This way, the wind flow that approaches the building roof will for a larger part flow over and around the roof rather than being forced through it. This phenomenon is called the wind-blocking effect. It was first identified by Blocken and Carmeliet in 2006 [38] in

their investigations of wind-driven rain deposition on buildings. Later, Blocken et al. [24-26] showed this effect to dominate over the so-called venturi-effect for wind flow in passages between buildings. These two effects also occur for the venturi-shaped roof. The venturi-effect refers to the increase of the wind speed in the roof due to the flow contraction. The wind-blocking effect refers to the decrease of the wind speed in the roof due to the increased resistance in the roof contraction. For the configuration without guiding vanes, it can be said that the venturi-effect dominates over the wind-blocking effect, yielding indeed a strong increase of the wind speed in the contraction and a strong negative underpressure. For the configurations with guiding vanes however, the wind-blocking effect seems to dominate over the venturi-effect: the increase of wind speed in the roof contraction is almost absent ($U/U_{ref} \approx 1$, see Fig. 11), and the resulting pressure coefficients are very low and might even become positive (overpressure).

In this respect, it is worthwhile to compare the performance of the three different roof configurations A, B and C with that of the reference configuration D, i.e. a building without venturi-shaped roof (see Fig. 2 and Fig. 7g-h). The C_p values at position E are compared in Table 1. The results show that the venturi-shaped roof without guiding vanes has a very good performance in terms of generating a strong underpressure coefficient. On the other hand, including guiding vanes has a negative effect: it cancels the positive effect of the venturi-shaped roof and generally leads to a performance that is even less than that without venturi-shaped roof. This means that for the configuration without guiding vanes, the term "venturi-roof" could be used with some justification, while this justification seems absent for the configurations with guiding vanes. In that case, the terminology should be restricted to "venturi-shaped roof".

It is important to mention the limitations of the present study. This study has focused on three different venturi-shaped roof designs. However, it has been conducted for only one set of parameters b, c, g and f (see Fig. 1). It has also only been conducted for one building geometry (L x B x H = 20 m x 20 m x 50 m) and without explicitly including the effect of surrounding buildings. Note that the effect of (distant) urban surroundings was included using an aerodynamic roughness length $y_0 = 0.5$ m (full scale value). Finally, the present study did not model the exhaust air flow coming from the building zones and being extracted by the generated underpressure. Therefore, further research should focus on at least the following important issues:

- Optimization of the performance of the venturi-shaped roof by the optimum combination of parameters b and c;
- Analysing the influence of the overall building dimensions (L, B, H) on the performance of the venturi-shaped roof;
- Analysing the influence of the approach-flow profile (y_0 value) on the roof performance;
- Analysing the influence of explicitly modelled urban surroundings (neighbouring buildings) on the roof performance;
- Analysing the performance of the venturi-shaped roof including the discharge of exhaust air in the roof contraction.

The present and future research efforts are intended to support the design of new buildings with a venturi-shaped roof to drive the natural ventilation of the building zones. Given the importance of exposure of the building roof to the oncoming wind, this roof concept will typically be applied for medium-rise and/or high-rise buildings, or for low-rise buildings without significant nearby obstructions. More information about the integration of this roof concept into a larger framework of sustainable building design can be found in [2].

7. Conclusions

In this study, Computational Fluid Dynamics (CFD) and wind tunnel experiments have been used to analyse the wind flow conditions in a venturi-shaped roof, with focus on the underpressure in the narrowest roof section (contraction). This underpressure can be used to partly or completely drive the natural ventilation of the building zones. The following conclusions have been obtained:

- The 3D CFD simulations were performed with special care for high-quality grid generation, specification of consistent boundary conditions and comparison with detailed wind tunnel measurements.
- The 3D steady RANS CFD simulations with the RNG k-ε model show a good agreement with the wind tunnel measurements for the mean wind speed ratio inside the roof. For the surface pressures inside the roof, the agreement is less good, but this less agreement does not compromise the evaluation of the different design configurations.
- The following different design configurations of the venturi-shaped roof have been analysed: without guiding vanes, with guiding vanes at every 90° interval and with guiding vanes at every 10° interval.
- The configuration without guiding vanes strongly outperforms the other configurations in terms of the magnitude of the underpressure in the roof contraction. The reason is that adding guiding vanes strongly increases the flow resistance, which causes a larger part of the approaching wind flow to flow over and around the roof, rather than being forced through it. This phenomenon has been called wind-blocking effect in previous studies.

- The wind-blocking effect causes the – at least at first sight – strange observation that the venturi-shaped roof with guiding vanes performs worse than the configuration without venturi-shaped roof.
- For the configuration without guiding vanes, the venturi-effect dominates over the wind-blocking effect. Indeed, due to the flow contraction, the mean wind speed in the contraction and the resulting underpresssure are strongly augmented. This is in line with the definition of the venturi-effect (i.e. increase in fluid speed due to flow contraction) and therefore provides justification to call the roof not only a "venturi-shaped roof" but also a "venturi-roof".
- For the configurations with guiding vanes, the wind-blocking effect dominates over the venturi-effect, and the roof can be called "venturi-shaped roof" but should not be called a "venturi-roof".
- The results of this study only apply for the roof and building configurations studied here. Further research is needed to expand the validity of the present findings, especially concerning the balance between the venturi-effect and the wind-blocking effect.

References

[1] Khan N, Su Y, Riffat SB. A review on wind driven ventilation techniques. Energy Build 2008;40(8), 1586-1604.
[2] Bronsema B. Earth, Wind & Fire – Air-conditioning powered by nature. 10th REHVA World Congress CLIMA 2010, 9-12 May, Antalya, Turkey.
[3] Chen Q. Ventilation performance prediction for buildings: A method overview and recent applications. Build Environ 2009;44(4) 848-858.
[4] Linden PF. The fluid mechanics of natural ventilation. Annu Rev Fluid Mech 1999;31: 201-238.
[5] Hunt GR, Linden PF. The fluid mechanics of natural ventilation - displacement ventilation by buoyancy-driven flows assisted by wind. Build Environ 1999;34(6): 707-720.
[6] Heiselberg P, Li Y, Andersen A, Bjerre M, Chen Z. Experimental and CFD evidence of multiple solutions in a naturally ventilated building. Indoor Air 2004;14(1): 43-54.
[7] Li YG, Delsante A. Natural ventilation induced by combined wind and thermal forces. Build Environ 2001;36(1): 59-71.
[8] Costola D, Blocken B, Hensen JLM. Overview of pressure coefficient data in building energy simulation and airflow network programs. Build Environ 2009;44(10): 2027-2036.
[9] Costola D, Blocken B, Ohba M, Hensen JLM. Uncertainty in airflow rate calculations due to the use of surface-averaged pressure coefficients. Energy Build 2010;42(6): 881-888.
[10] Tsutsumi J, Katayama T, Ishii A, He P, Hayashi T. Investigation and numerical simulation of the wind effects on thermal comfort in a house. J Wind Eng Ind Aerod 1996;60(1-3): 267-280.
[11] Gao NP, Niu JL, Perino M, Heiselberg P. The airborne transmission of infection between flats in high-rise residential buildings: Tracer gas simulation. Build Environ 2008;43(11): 1805-1817.
[12] Tablada A, de Troyer F, Blocken B, Carmeliet J, Verschure H. On natural ventilation and thermal comfort in compact urban environments - the Old Havana case. Build Environ 2009;44(9): 1943-1958.
[13] van Hooff T, Blocken B. Coupled urban wind flow and indoor natural ventilation modelling on a high-resolution grid: A case study for the Amsterdam ArenA stadium. Environ Modell Softw 2010;25(1): 51-65.
[14] Jiang Y, Alexander D, Jenkins H, Arthur R, Chen Q. Natural ventilation in buildings: Measurement in a wind tunnel and numerical simulation with large-eddy simulation. J Wind Eng Ind Aerod 2003;91(3) 331-353.
[15] Karava P, Stathopoulos T, Athienitis AK. Wind-induced natural ventilation analysis. Sol Energy 2007;81(1): 20-30.
[16] Karava P, Stathopoulos T, Athienitis AK. Airflow assessment in cross-ventilated buildings with operable facade elements. Build Environ 2011;46(1): 266-279.
[17] Bu Z, Kato S, Takahashi T. Wind tunnel experiments on wind-induced natural ventilation rate in residential basements with areaway space. Build Environ 2010;45(10): 2263-2272.
[18] Norton T, Grant J, Fallon R, Sun DW. Assessing the ventilation effectiveness of naturally ventilated livestock buildings under wind dominated conditions using computational fluid dynamics. Biosystems Engineering 2009;103(1): 78-99.
[19] Norton T, Grant J, Fallon R, Sun DW. Optimising the ventilation configuration of naturally ventilated livestock buildings for improved indoor environmental homogeneity. Build Environ 2010;45(4): 983-995.
[20] van Hooff T, Blocken B. On the effect of wind direction and urban surroundings on natural ventilation of a large semi-enclosed stadium. Comput Fluids 2010;39(7): 1146-1155.
[21] Blocken B, Stathopoulos T, Carmeliet J, Hensen JLM. Application of CFD in building performance simulation for the outdoor environment: an overview. Journal of Building Performance Simulation 2011; in press. doi: 10.1080/19401493.2010.513740

[22] Chikamoto T, Kato S, Ikaga T. Hybrid air-conditioning system at Liberty Tower of Meiji University. First International One day Forum on Natural and Hybrid Ventilation (HybVent Forum'99), Sydney, Australia, 1999.

[23] Sauerbruch M, Hutton L. 2000. GSW headquarters Berlin. Lars Müller, Berlin, 2000.

[24] Blocken B, Carmeliet J, Stathopoulos T. CFD evaluation of the wind speed conditions in passages between buildings – effect of wall-function roughness modifications on the atmospheric boundary layer flow. J Wind Eng Ind Aerod 2007;95(9-11): 941-962.

[25] Blocken B, Stathopoulos T, Carmeliet J. Wind environmental conditions in passages between two long narrow perpendicular buildings. J Aerospace Eng–ASCE 2008;21(4): 280-287.

[26] Blocken B, Stathopoulos T, Carmeliet J. A numerical study on the existence of the Venturi-effect in passages between perpendicular buildings. J Eng Mech-ASCE 2008;134(12): 1021-1028.

[27] Franke J, Hellsten A, Schlünzen H, Carissimo B (Eds.). Best practice guideline for the CFD simulation of flows in the urban environment. COST Office Brussels; 2007.

[28] Tominaga Y, Mochida A, Yoshie R, Kataoka H, Nozu T, Yoshikawa M, Shirasawa T. AIJ guidelines for practical applications of CFD to pedestrian wind environment around buildings. J Wind Eng Ind Aerod 2008;96(10-11): 1749-61.

[29] van Hooff T, Blocken B, van Harten M. 3D CFD simulations of wind flow and wind-driven rain shelter in sports stadia: influence of stadium geometry. Build Environ 2011;46(1): 22-37.

[30] Launder BE, Spalding DB, The numerical computation of turbulent flows. Comput Method Appl M 1974;3: 269-289.

[31] Cebeci T, Bradshaw P. Momentum transfer in boundary layers, Hemisphere Publishing Corporation; 1977.

[32] Fluent Inc. Fluent 6.3. User's Guide. Fluent Inc., Lebanon; 2006.

[33] Blocken B, Stathopoulos T, Carmeliet J. CFD simulation of the atmospheric boundary layer: wall function problems. Atmos Environ 2007;41(2): 238-252.

[34] Yakhot V, Orszag SA, Thangam S, Gatski TB, Speziale CG. Development of turbulence models for shear flows by a double expansion technique. Physics of Fluids 1992;A4: 1510-1520.

[35] Evola G, Popov V. Computational analysis of wind driven natural ventilation in buildings. Energy Build 2006;38(5): 491-501.

[36] Murakami S. Comparison of various turbulence models applied to a bluff body. J Wind Eng Ind Aerod 1993;46 & 47: 21-36.

[37] Tominaga Y, Mochida A, Murakami S, Sawaki S. Comparison of various revised k–ε models and LES applied to flow around a high-rise building model with 1:1:2 shape placed within the surface boundary layer. J Wind Eng Ind Aerod;96 (4), 389-411.

[38] Blocken B, Carmeliet J. The influence of the wind-blocking effect by a building on its wind-driven rain exposure. J Wind Eng Ind Aerod 2006;94(2): 101-127.
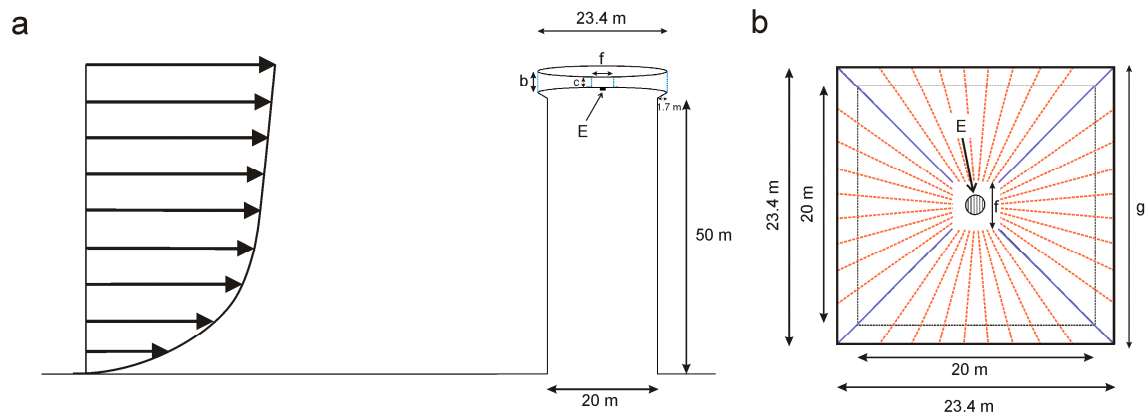
Fig. 1: Geometry of the building used for the wind tunnel experiments and the CFD simulations (a) Vertical cross-section showing the building with the square disk-shaped roof (not to scale) and position E where the surface pressure is evaluated. (b) Horizontal cross-section of the roof. The solid blue lines represent the guiding vanes positioned at every 90° interval, the dashed orange lines indicate the positions of the guiding vanes at every 10° interval.
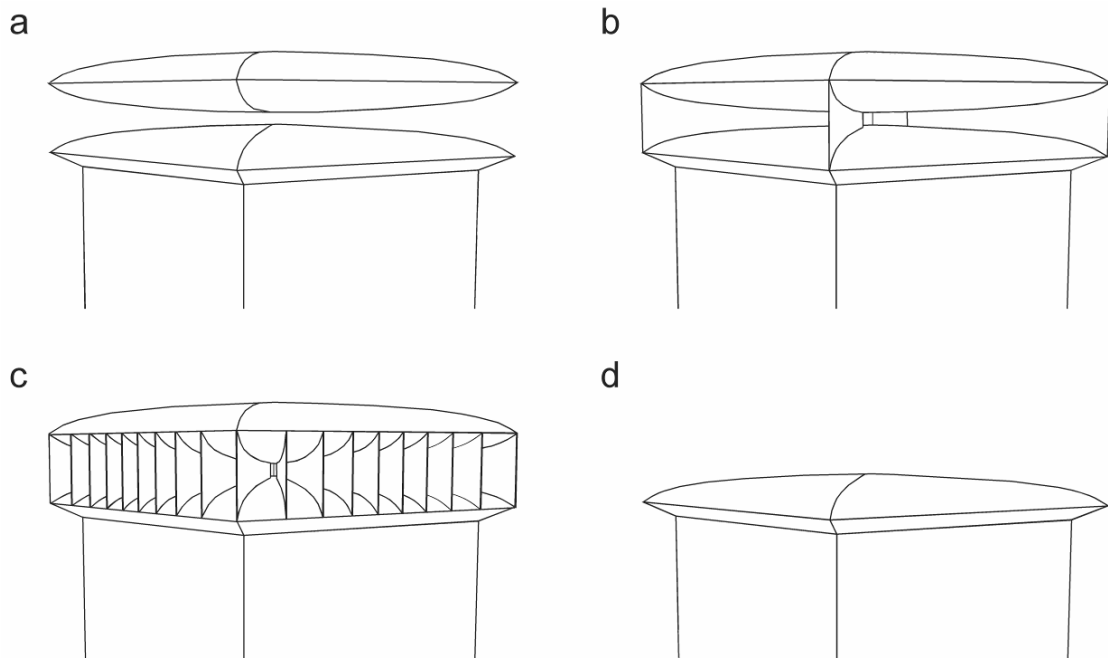

Fig. 2: (a) Venturi-shaped roof configuration without guiding vanes; (b) configuration with guiding vanes every 90°; (c) configuration with guiding vanes every 10°. (d) Reference configuration without venturi-shaped roof.

9
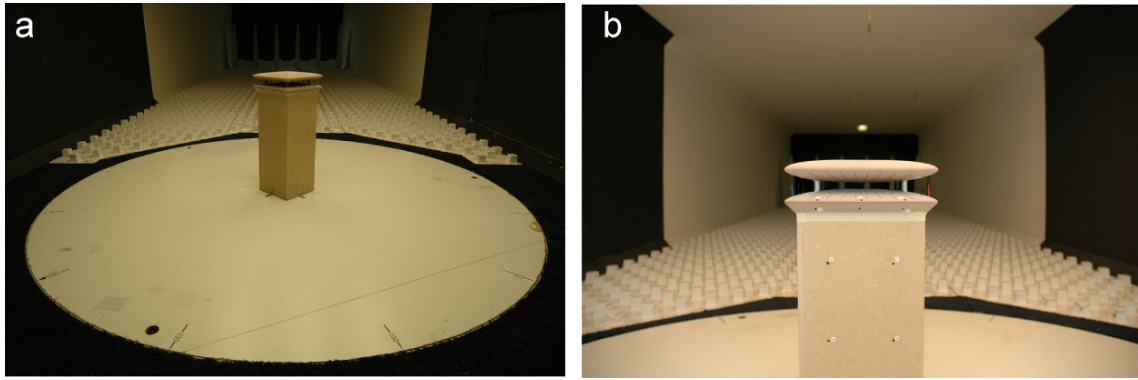
Fig. 3: Pictures of the building model in the closed-circuit ABL wind tunnel at Peutz BV. (a) View of the upstream domain with building model positioned in the middle of the turntable for wind direction of 45°. (b) Close-up view of the building showing some of the leeward facade locations of the surface pressure measurements (see also Fig. 4).
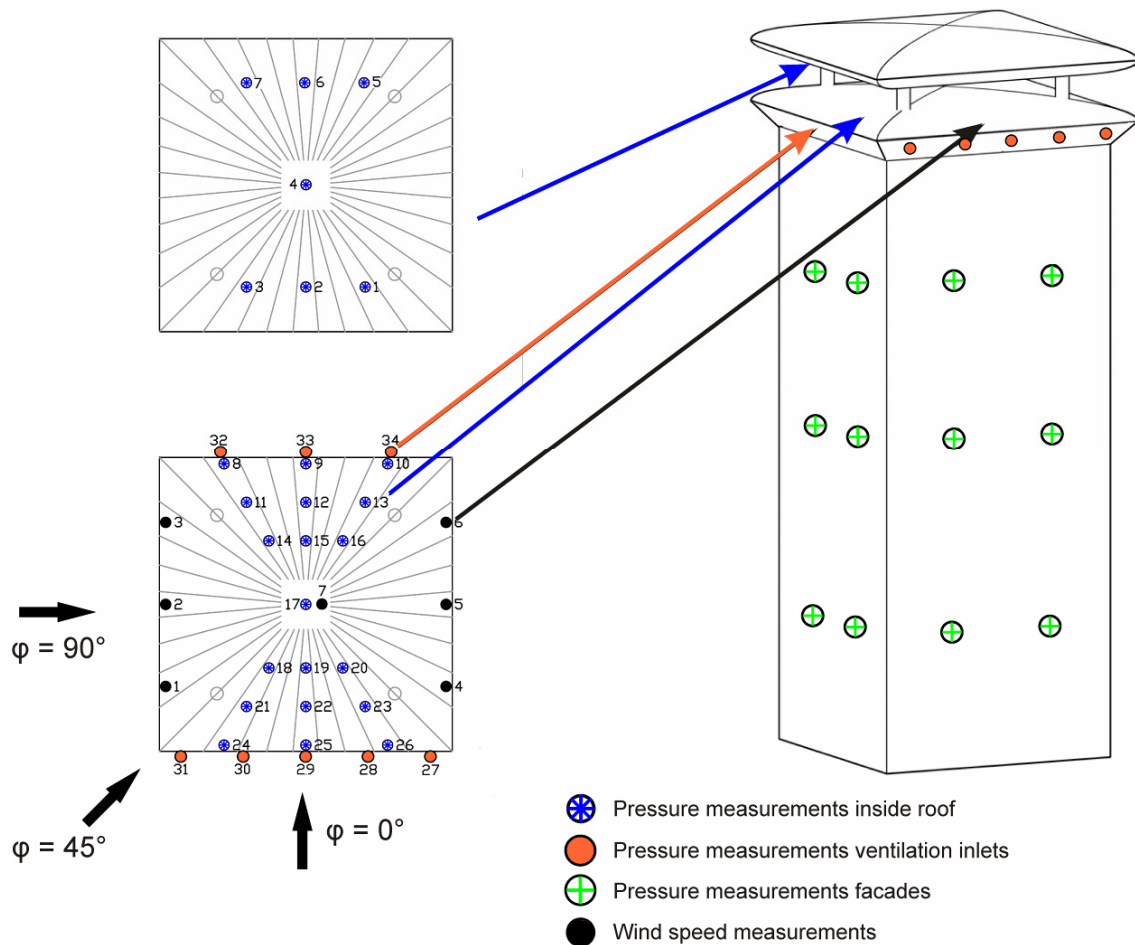
Fig. 4: Schematic view of the building model with indication of the measurement positions. The blue (star-type) symbols indicate the positions of the surface pressure measurements inside the roof, the solid red symbols indicate the positions of the surface pressure measurements at the ventilation inlets of the building, the green (cross-type) symbols indicate the position of the surface pressure measurements on the facades. Finally, the solid black symbols indicate the position of the wind speed measurements, which are performed at mid-height inside the roof contraction.
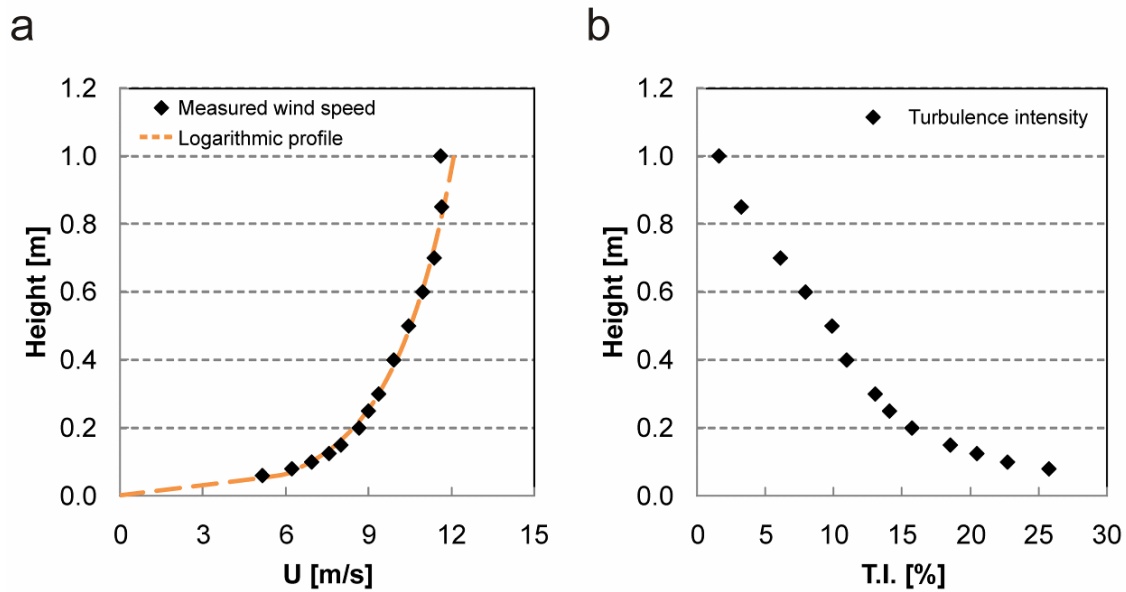
Fig. 5: (a) Measured approach-flow mean wind speed profile along a vertical line at the upstream edge of the turntable. It closely resembles a log law profile with $u^* = 0.956$ m/s and $y_0 = 0.005$ m (full–scale $y_0 = 0.5$ m). (b) Measured turbulence intensity T.I. along the same vertical line.
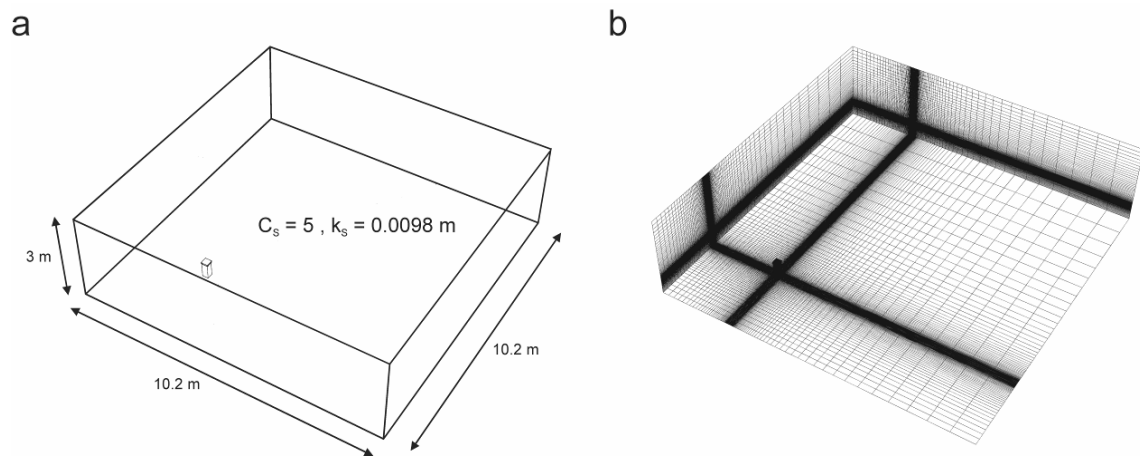

Fig. 6: (a) Perspective view of the building in its computational domain at model scale. (b) View of the computational grid at some of the domain surfaces.
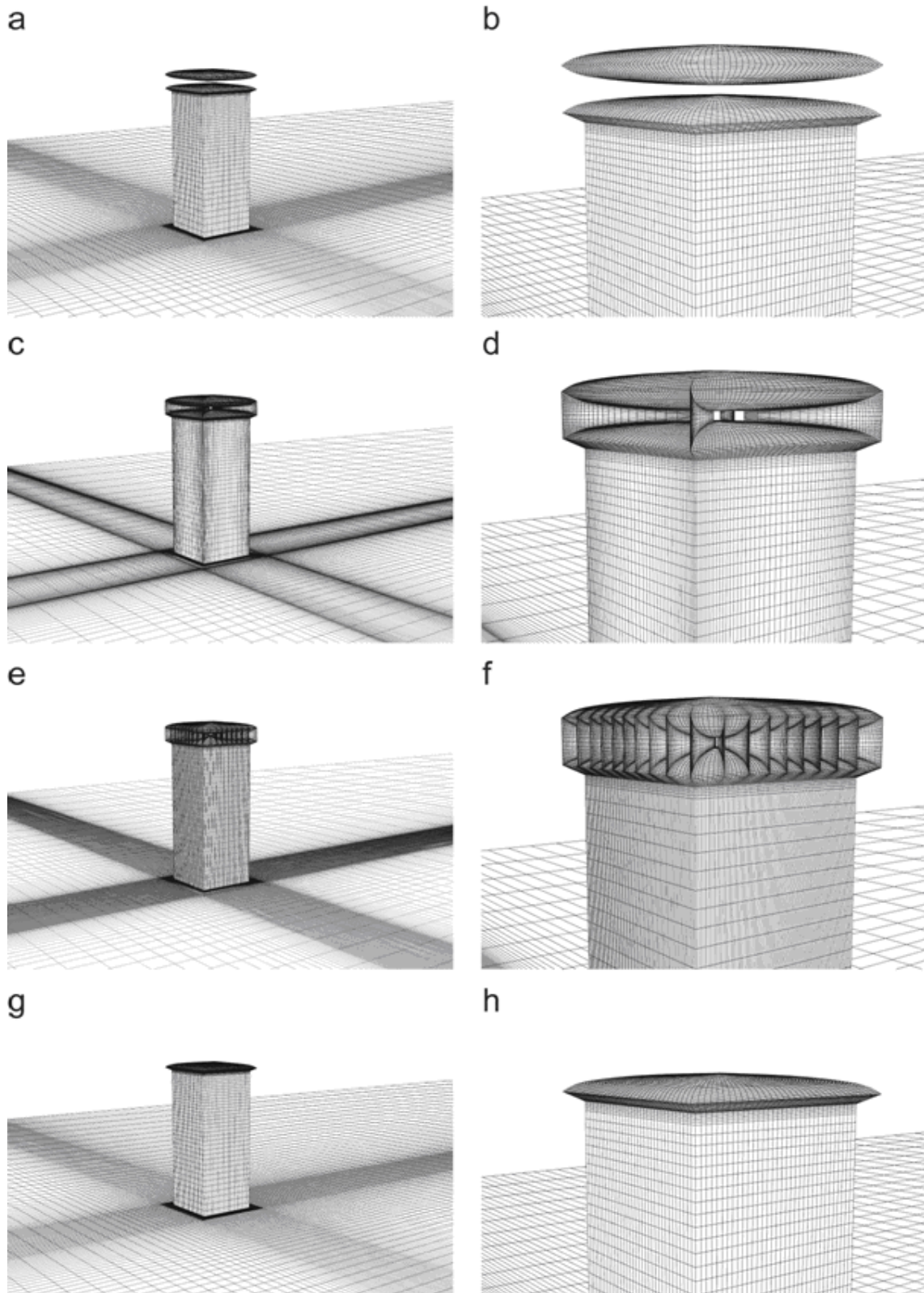
Fig. 7: Computational grids for the three different design configurations and the reference configuration: (a,b) no guiding vanes (2,0 million cells); (c,d) guiding vanes every 90° (2,4 million cells); (e,f) guiding vanes every 10° (3.3 million cells); (g,h) no venturi-shaped roof (1.8 million cells).
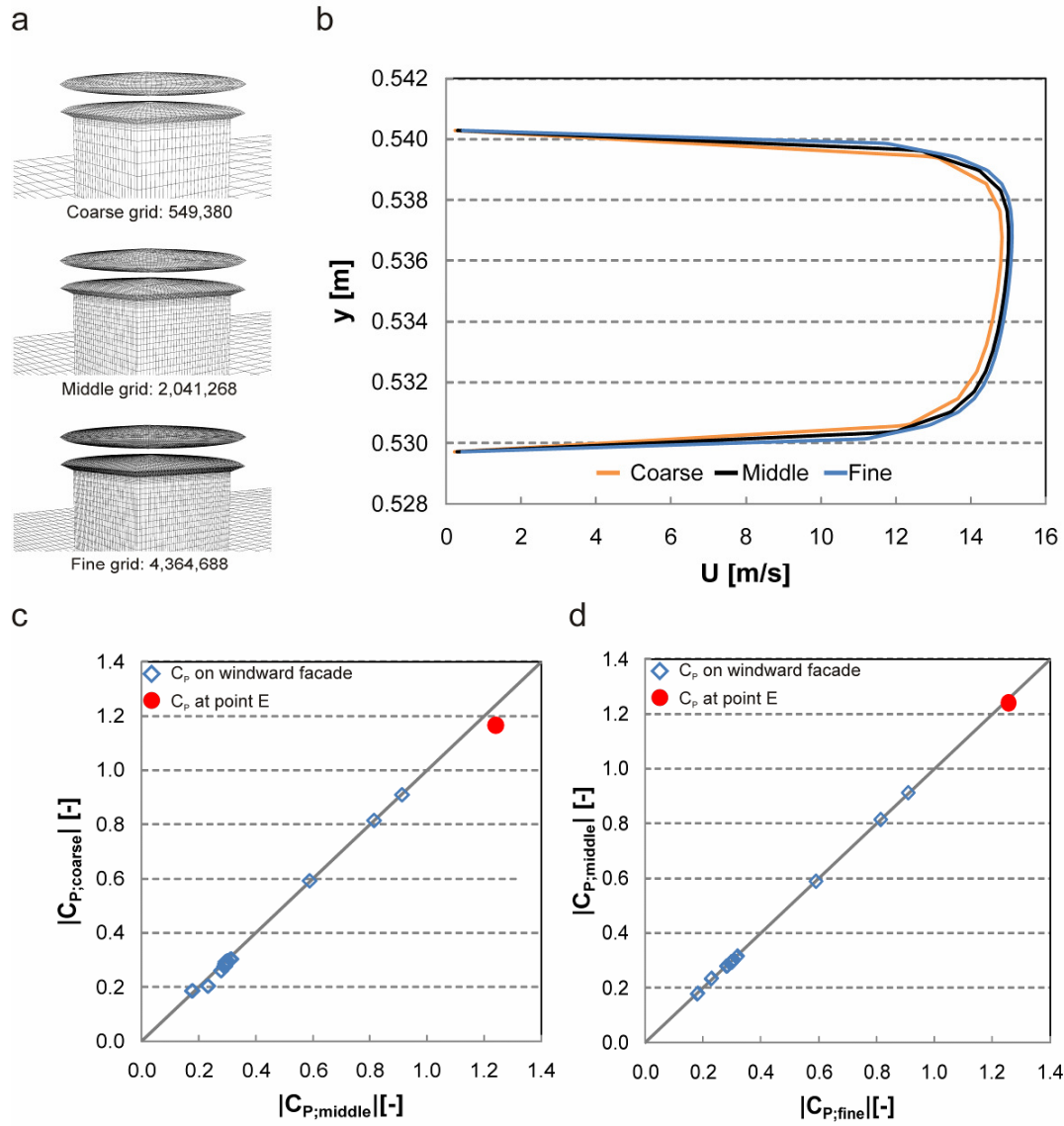
Fig. 8: Grid-sensitivity analysis for configuration A (no guiding vanes) and φ = 0°. (a) View of the three computational grids: coarse grid (549,380 cells), middle grid (2,041,268 cells) and fine grid (4,364,688 cells). (b) Mean wind speed profile for the three grids along a vertical line in the centre of the roof contraction. (c) Comparison of pressure coefficients obtained with the coarse grid and the middle grid. (d) Comparison of pressure coefficients obtained with the middle grid and the fine grid.
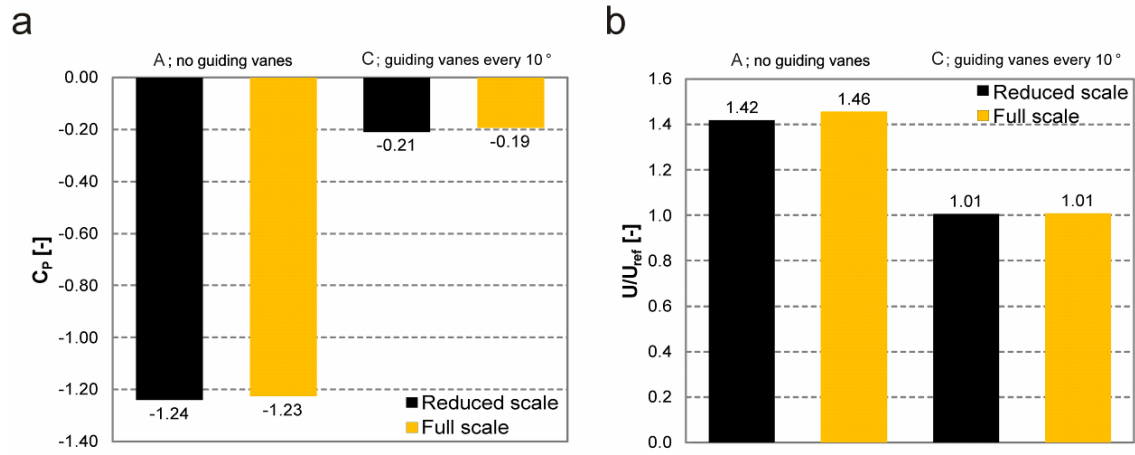
Fig. 9: Comparison between results obtained from CFD simulations with the reduced-scale model and the full-scale model for configurations A and C and for a wind direction φ = 0°. (a) Comparison of pressure coefficient at position E. (b) Comparison of wind speed ratio U/U$_{ref}$ at mid-height in the centre of the roof contraction.
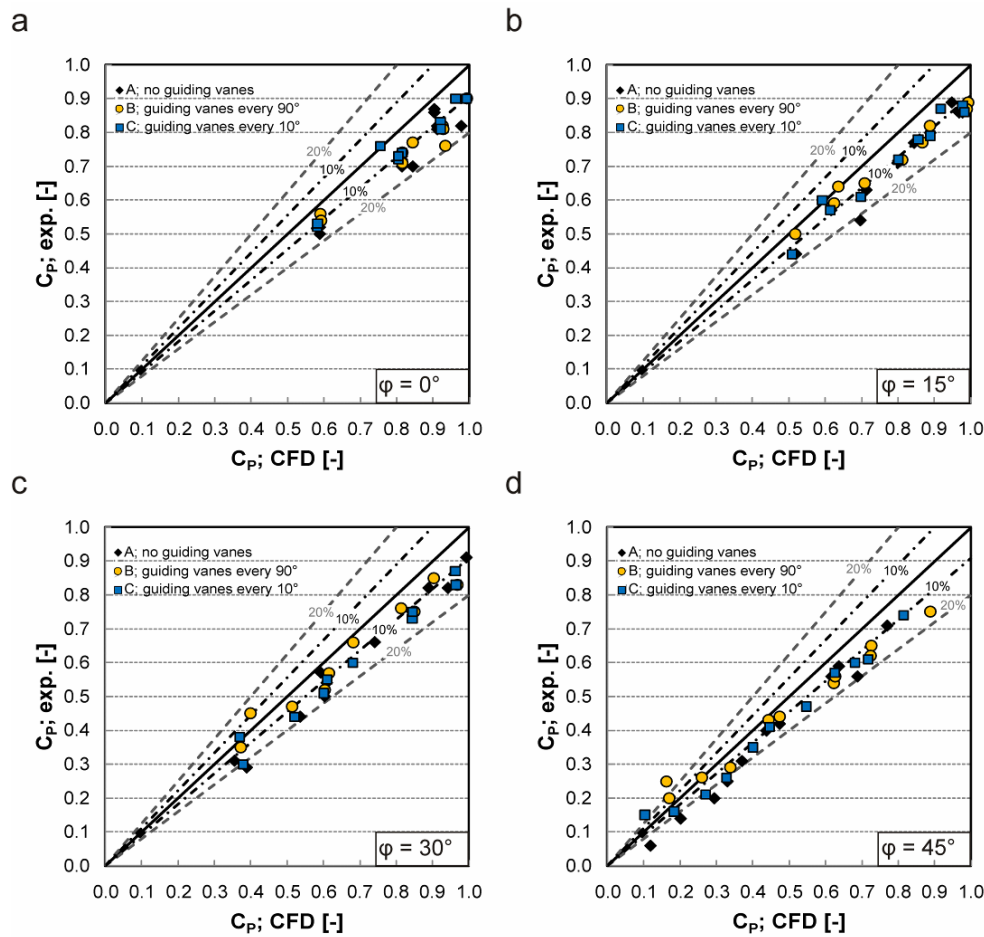

Fig. 10: Comparison between numerically simulated and measured pressure coefficients C$_P$ on the windward facades and the windward ventilation inlet of the building for the roof configurations A, B, C and for the four wind directions: (a) φ = 0°; (b) φ = 15°; (c) φ = 0°; (d) φ = 45°.
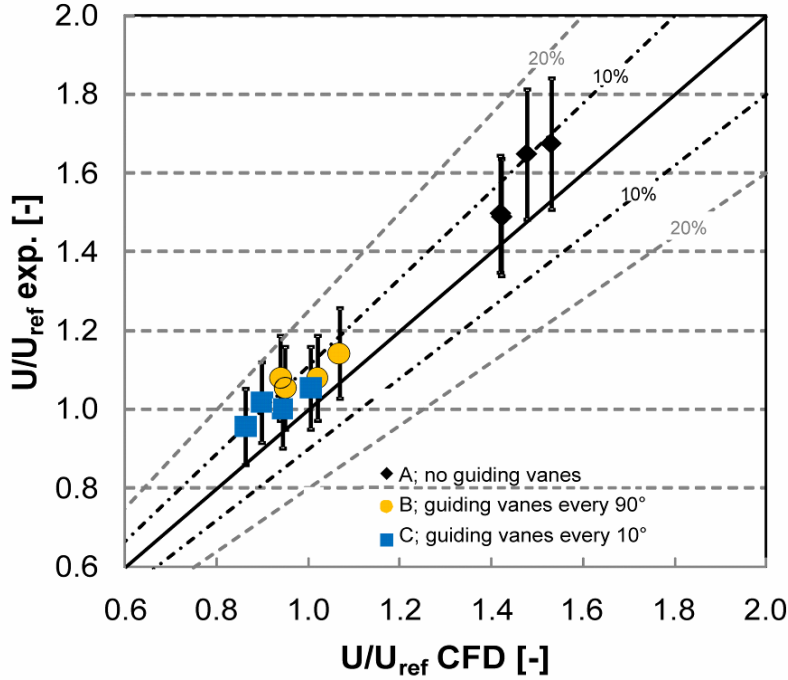
14

Fig. 11: Comparison between numerically simulated and measured velocity ratio U/U_{ref} at mid-height in the centre of the roof contraction for the roof configurations A, B, C and for the four wind directions ($\varphi = 0°$, 15°, 30°, 45°). The error bars represent the measuring accuracy of ±10%.
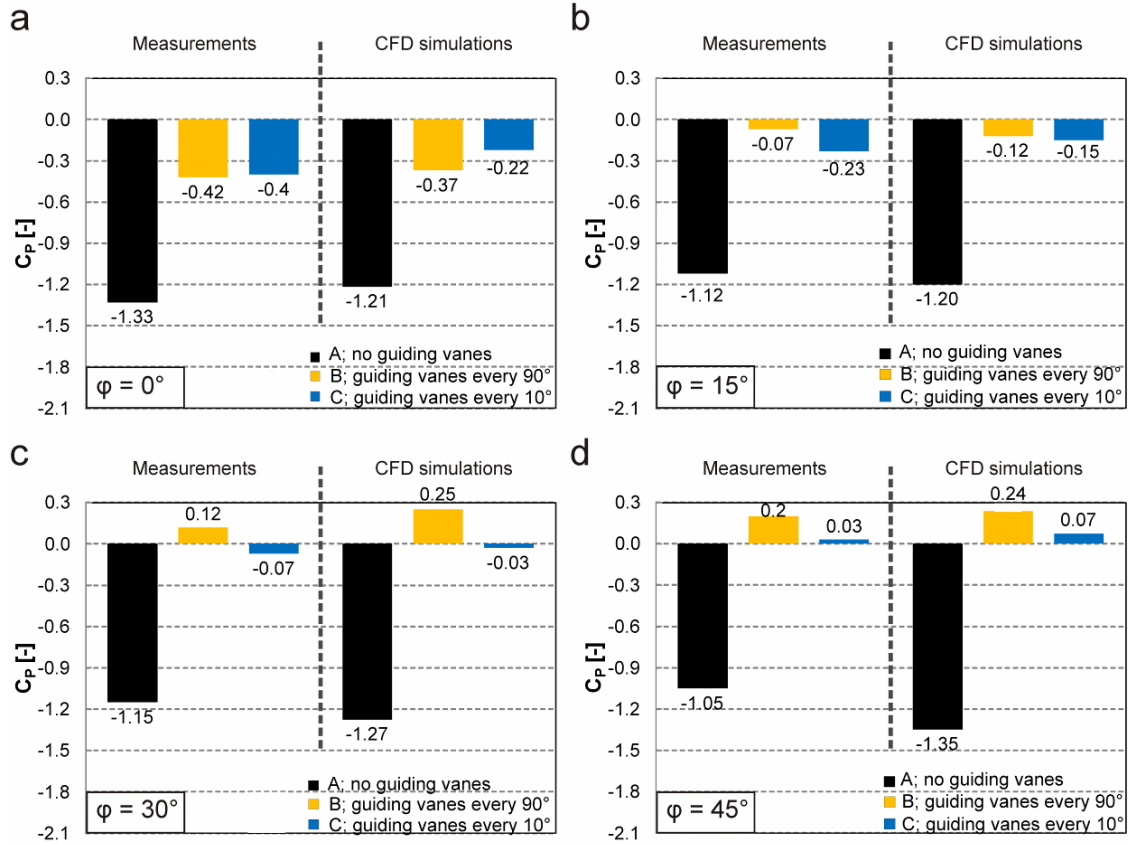

Fig. 12: Comparison between numerically simulated and measured pressure coefficients C_P at position E for the roof configurations A, B, C and for the four wind directions: (a) $\varphi = 0°$; (b) $\varphi = 15°$; (c) $\varphi = 30°$; (d) $\varphi = 45°$.